Comparison of MHD-induced rotation damping with NTV predictions on MAST

M-D Hua[1,2], IT Chapman[2], AR Field[2], RJ Hastie[2], SD Pinches[2] and the MAST Team[2]

[1]Imperial College, Prince Consort Road, London SW7 2'BY, United Kingdom
[2]EURATOM/CCFE Fusion Association, Culham Science Centre, Abingdon, Oxfordshire OX14 3DB, United Kingdom

E-mail: minh-duc.hua@polytechnique.org

Abstract. Plasma rotation in tokamaks is of special interest for its potential stabilising effect on micro- and macro instabilities, leading to increased confinement. In MAST, the torque from Neutral Beam Injection (NBI) can spin the plasma to a core velocity $\sim 300\text{km.s}^{-1}$ (Alfvén Mach number ~ 0.3). Low density plasmas often exhibit a weakly non-monotonic safety factor profile just above unity. Theory predicts that such equilibria are prone to Magneto-Hydro-Dynamic (MHD) instabilities, which was confirmed by recent observations. The appearance of the mode is accompanied by strong damping of core rotation on a timescale much faster than the momentum confinement time.

The mode's saturated structure is estimated using the CASTOR code together with Soft X-Ray measurements, enabling the calculation of the plasma braking by the MHD mode according to Neoclassical Toroidal Viscosity theory. The latter exhibits strong similarities with the torque measured experimentally.

1. Introduction

Plasma rotation has recently received growing interest as it proved beneficial in achieving better confinement in tokamaks [1]. On a micro-scale, the resulting $E \times B$ flow shear helps suppress the turbulence [2,3], while on the macro-scale, rotation exerts a stabilising effect on Magneto-Hydro-Dynamic (MHD) modes. This is observed for a large range of instabilities, including the ballooning mode [4–8], the internal kink mode [9, 10] and the sawtooth instability [11–13].

Advanced scenarios for plasma operation being presently developed for ITER [14–18] aim at high fusion gains and steady state operation. They rely on an optimised self generated plasma current, the so-called bootstrap-current [19], to produce steady-state discharges. In the hybrid scenario [20, 21], a broad low shear or weakly reversed shear safety factor (q) profile is used towards this goal, the magnetic shear being defined here as $s = rq^{-1}dq/dr$. Such safety factor profiles also have a minimum value just above 1, which prevents the appearance of the sawtooth instability, detrimental for plasma confinement. In high performance plasmas however, this scenario suffers from the Resistive Wall Mode (RWM) arising from the interaction of a pressure-driven external kink instability with the tokamak wall [22]. A relevant performance measure is the plasma β defined as $2\mu_0\langle p\rangle/B_0^2$, angled brackets denoting a flux surface average and B_0 the toroidal magnetic field at the magnetic axis. Sustaining high toroidal rotation is of importance when dealing with the RWM, since it is one of the ways of operating above the mode's β threshold [23–29], and helping achieve the targeted high pressures.

Over the past few years, a number of deleterious phenomena have been observed, whereby electromagnetic perturbations degrade plasma rotation, the latter change further amplifying the original instability, leading to a self-feeding process which destroys plasma confinement. This is observed at the edge of the plasma, where penetration of error-fields can occur [30], or in the triggering process for Edge Localised Modes [31]. It can also affect the whole plasma, for example in the form of mode locking [32], the drag being associated with mode-induced eddy currents penetrating into the tokamaks coils and vessel. Such effects with far-reaching consequences on plasma performance justify the investigation of the interplay between MHD activity and plasma rotation.

Neutral Beam Injection (NBI) in MAST provides ideal conditions for such studies. The torque it provides spins the plasma core up to velocities $\sim$ 300km.s^{-1} which corresponds to a core Alfvén Mach number ~ 0.3. The latter is defined as the ratio of the plasma velocity to the Alfvén velocity, $M_A = v_\phi B_0^{-1}\left(\mu_0\rho\right)^{1/2}$, with v_ϕ the toroidal plasma velocity and ρ its mass density. The increased core temperature resulting from the NBI heating slows down current diffusion, producing a hybrid-like, broad low shear or weakly reversed shear q profile just above 1. Equilibria with such q profiles are predicted to be prone to saturated ideal MHD instabilities when the minimal q value, q_{min}, approaches an integer value [33–36]. This type of instability is indeed observed in MAST when $q_{min} \sim 1$ [37, 38] and is referred to as Long-Lived Mode (LLM).

Following the onset of the LLM, strong damping of core rotation is observed on a

timescale much shorter than that of momentum transport (figure 1). During this phase, the mode angular frequency does not evolve significantly. After the plasma angular frequency profile has become flat, both the rotation of the plasma and that of the mode gradually decrease.

This study focuses on the initial flattening of the rotation profile. Its short timescale compared to that of momentum transport implies that the braking of the plasma does not arise from MHD-enhanced momentum transport. The LLM causes fast ion losses and redistribution, which affects rotation. Initial calculations indicate that the torque associated with this effect is significantly smaller than that needed to produce the observed braking. Further calculations using the HAGIS drift kinetic code [39] will be performed to assess the effect of the fast ion redistribution on rotation in the future. High resolution temperature measurements using Thomson Scattering (TS) do not show any local profile flattening characteristic of magnetic islands. Additionally, no π phase-jumps are observed between neighbouring channels of poloidal cross-section Soft X-Ray cameras (SXR). These phase jumps are another indication of magnetic reconnection, and are indeed observed in MAST in the presence of Neoclassical Tearing Modes (NTM). This does not only corroborate the ideal-MHD nature of the mode, but also rules out resonant electromagnetic torques associated with reconnection as a mechanism for plasma braking [40, 41]. Electromagnetic torques can act on the plasma even in the absence of magnetic islands [42]. They are nevertheless strongly localised around the Alfvén resonances, in the vicinity of the minimal and integer q locations, inconsistent with the collapse of the whole rotation profile caused by the LLM. In plasmas featuring the LLM, the innermost Alfvén resonance is located around mid-radius, meaning that electromagnetic torques would result in a maximal damping outside the core of the plasma, in contradiction with the observations. Significantly affecting core rotation with these torques would require a diffusion about an order of magnitude higher than observed before mode onset, and the resulting damping profile would still not be peaked in the core, as seen in the experiment. In contrast, the torque arising from Neoclassical Toroidal Viscosity (NTV) [43] is distributed and occurs on a thermal ion collision time scale ($\sim 10^{-4}$s), thus appearing well suited to describe the measured braking of the plasma by the LLM.

The research presented here investigates whether the torque predicted by NTV theory is consistent with the observed damping of core rotation following the LLM onset. The structure of the LLM is first determined using the CASTOR linear code [44], its saturated amplitude is then estimated by comparing results of forward simulations of the SXR emission to the measurements. This is detailed in section 2. Based on this information, the NTV torque is calculated and compared to experimental data, a process which is explained in section 3. Figure 2 summarises the rationale of the analysis described through sections 2 and 3. Section 4 presents results of experiments carried out on MAST, while section 5 draws conclusions.

2. Structure of the MHD mode

The structure of the LLM is investigated using the CASTOR code (section 2.1). It is a linear code, therefore giving the eigenstructure of the most unstable mode, but without any information on the saturation amplitude. MHD modes can be observed on the SXR diagnostic (section 2.2), which can yield an estimate of the saturated amplitude. This is done, given the eigenstructure calculated by CASTOR, by simulating the observed SXR fluctuations for a range of assumed amplitudes and selecting the best agreement with the experimental data (section 2.3 and 2.4). The upper part of figure 2 summarises this process.

2.1. Eigenstructure analysis from the CASTOR code

The equilibria analysed here are reconstructed using the EFIT code [45], constrained to magnetic field pitch-angle data from the Motional Stark Effect diagnostic (MSE), as well as total pressure data measured by TS, Charge eXchange Recombination Spectroscopy (CXRS) and bremsstrahlung measurements. This enables an accurate calculation of the q profile of the discharge (figure 3). The CASTOR code requires the equilibrium input to be calculated by the HELENA code [46], a fixed boundary Grad-Shafranov equation solver employing the same straight field line coordinates as in the linear stability analysis. The HELENA equilibrium is adjusted to match the q profile reconstructed by EFIT.

Theory predicts the broad low shear or reversed shear equilibria studied to be unstable to ideal modes [33]. In addition, experimental observations do not give any evidence of the presence of reconnection, neither in the form of local flattening of high resolution TS electron temperature profiles, nor in the form of π phase-jumps in neighbouring channels of poloidal cross-section SXR cameras (section 2.2). The resistivity in CASTOR is therefore set to zero. Although the MHD mode analysed here was shown to interact with fast ions [38], this effect was not modelled while using CASTOR. The stability analysis is done in full toroidal geometry, taking into account plasma shaping. For a given toroidal n number, it assumes a spectrum of poloidal m numbers with $m \leq 30$, a spectrum broad enough to represent core instabilities. The equilibrium at mode onset reconstructed by the HELENA code is found to be unstable to an $n = 1$ ideal internal mode, consistent with [33].

2.2. Observation of MHD on SXR

In the case of MAST's horizontal SXR cameras array, the lines of sight along which the light is collected are located on a poloidal cross section, at a fixed toroidal position (figures 4 and 5). In the frequency range of the cameras, the SXR emissivity of the plasma is given by [48]:

$$\epsilon_{SXR} \;\alpha\; \frac{n_e n_i Z_{eff}^2}{\sqrt{T_e}} \int e^{-h\nu/eT_e} d\nu \tag{1}$$

where n_e, n_i, Z_{eff}, e, T_e and ν are respectively the electron density, ion density, effective ion charge, the elementary charge, electron temperature in eV and frequency of emission. Equation 1 shows that the SXR emissivity is predominantly dependent on T_e and increases with it. In the case of a non axisymmetric plasma, as the magnetic structure advected by the plasma motion flows past the cameras (figure 5), the temperature perturbation associated with the magnetic structure results in the fluctuation of the SXR signal in time, allowing the observation of MHD on SXR measurements. SXR data exhibits an additional feature when a magnetic island is present in the plasma: a characteristic π phase jump is observed between the two neighbouring lines of sight viewing opposite sides of the island. This is because the temperature perturbation changes sign across the island, and consequently the two lines of sight measure fluctuations of opposite sign [47]. Such π phase jumps are observed in MAST in the presence of NTMs, but not in plasmas with the LLM. Note however that if an island were present and led to local impurity accumulation, the resulting parasitic line-emission would screen the phase jump and would thus prevent the detection of the island.

2.3. Simulation of SXR measurements

Equation 1 is used to express the SXR emissivity as a function of poloidal flux, $\epsilon_{SXR} = f(\psi)$. Mid-plane TS measurements yield $T_e(\psi)$, $n_e(\psi)$ and $n_i(\psi)$ (assuming quasi-neutrality) and $Z_{eff}(\psi)$ is given by the analysis of bremsstrahlung emission on an equilibrium timescale.

The eigenstructure of the $n = 1$ ideal mode is given by CASTOR. Assuming an arbitrary amplitude makes it possible to calculate the poloidal flux perturbation for the entire three-dimensional plasma: $\delta\psi = f(R, \phi, Z)$ (with (R, ϕ, Z) the usual cylindrical coordinates). Added to the equilibrium flux, this provides the complete topology of the plasma flux surfaces, $\psi = f(R, \phi, Z)$, thus yielding a three-dimensional map of the SXR emissivity of the plasma: $\epsilon_{SXR} = f(R, \phi, Z)$.

The reconstruction described above is valid for a non-rotating magnetic structure. In reality, the structure moves toroidally due to plasma rotation, and its motion with respect to the plasma. In order for the MHD mode not to lose coherence, this motion has to be rigid rotation, such that $\psi = f(R, \phi + \omega t, Z)$, where ω is the angular frequency deduced from the experimental data by Fourier transform and t the time. The magnetic structure therefore moves across the camera plane located at $\phi = \phi_0$ and the SXR emission on that plane is $\epsilon_{SXR} = f(R, \phi_0 + \omega t, Z)$. This allows the integration of the SXR emission along the path of the camera line of sight, yielding the time-dependent simulation of the SXR measurements for an arbitrary toroidal mode number and mode amplitude.

2.4. Determination of the LLM saturated amplitude

Fourier analysis of the SXR fluctuations shows that from its onset until several tens of milliseconds later, the LLM does not feature any significant $n = 2$ component. Although the Mirnov coils spectrogram in figure 1 does show an $n = 2$ component, these coils measure the magnetic fluctuations outside the plasma, in contrast to the SXR cameras, which are able to observe the plasma core. In addition, it is likely that the $n = 2$ component in figure 1 arises as a non-linear consequence of the $n = 1$ mode. The absence of $n > 1$ modes is also expected from the stability analysis of the LLM [38]: the $n = 1$ component is unstable at larger q_{min} than the $n = 2$ component, and since the q profile evolves downwards during the discharge, the $n = 1$ component is always the only unstable at the appearance of the LLM, which is the phase analysed here. Consequently, we only consider the $n = 1$ component in the rest of this study.

The SXR signals are simulated for different mode amplitudes and compared to the experimental data. Since the MHD perturbation does not affect the average SXR signal but only results in its variation, this comparison is based on the SXR fluctuations only. This method reduces the influence of parasitic SXR sources, as for example impurity line emission. The simulation having the lowest residuals with respect to the measurements is then considered a good estimate of the mode amplitude. (Should it be necessary to include the $n = 2$ mode in the analysis, the simulation would be carried out with various $n = 1$ and $n = 2$ amplitudes, as well as toroidal phases between these components). It is assumed here that, as the instability saturates, its structure remains identical to the linear one. This assumption, although quite strong, is likely to hold outside the resonant surfaces and inertial layer of the mode [34, 49].

3. Torque according to NTV theory

The saturated MHD structure is determined as described in section 2. The braking it induces is calculated using Neoclassical Toroidal Viscosity theory. This theory is introduced in section 3.1 and a formulation applicable to MAST plasmas is presented in section 3.2.

3.1. NTV theory

NTV theory describes the damping of the plasma flow arising from the breaking of axisymmetry [43,50]. The underlying mechanism is most easily understood in collisional plasmas where the dissipation of toroidal angular momentum is similar to that occurring during magnetic pumping [51]. The presence of the magnetic perturbation results in the distortion of the plasma's flux tubes. Flux conservation prescribes parts of the flux tube with small cross-section to have a high magnetic field, hence a high perpendicular pressure by conservation of the first adiabatic invariant (the fluid cell contains the same particles over time, provided many collisions occur during its toroidal precession). If the collision time is short compared to the period of the fluid cell motion, constant total pressure on the flux surface indicates that the parallel pressure is low. Conversely, portions of the flux tube with large cross section have a low magnetic field, low perpendicular pressure and high parallel pressure. Therefore, as the fluid cell travels across the distorted flux tube, it experiences an oscillation of parallel and perpendicular pressures as well as of flux tube's shape. In such a system, the work done by the parallel and perpendicular pressure vanishes because the pressure and shape oscillations are in phase. The effect of collisions is however not instantaneous, and the oscillation of pressures lags that of shape, causing an overall braking of the fluid cell. This mechanism is sketched in figure 6. In the collisionless regime more relevant to tokamaks, the variation of the toroidal field results in a drift of the particles trapped in banana orbits. This gives rise to a radial current which exerts a $\boldsymbol{j} \times \boldsymbol{B}$ torque on the plasma.

A quantitative expression for the NTV force can be obtained by solving the drift-kinetic equation, then taking the velocity moment of the distribution function to obtain the radial flux, and eventually using the flux-friction relation derived from neoclassical theory [52,53] to obtain the plasma viscosity. This derivation is carried out in reference [43].

NTV theory has been applied extensively to externally-driven, static magnetic perturbation cases [54, 55]. This theory can also be used if the field's axisymmetry is broken by the presence of an MHD instability, in which case the torque arises from the differential flow of the plasma through the non-axisymmetric perturbation. In this case, the flow damping brings the rotation of the plasma into agreement with that of the magnetic structure (figure 7). The equivalence with the static case is found by moving from the lab frame to that traveling with the MHD instability, a frame change which is possible only because the mode has a rigid body rotation. The angular frequency

of this motion results from the interaction of the non-axisymmetric magnetic structure with both the plasma and the conducting external components of the tokamak. This frequency is measured experimentally, so that it is not necessary to calculate the external drag on the magnetic structure. The presence of this drag explains why the presence of the internal MHD mode not only leads to angular momentum density redistribution but also to an overall loss of momentum.

Since the magnetic perturbation is not applied externally, its structure has to be calculated using an MHD code. Although there are some uncertainties inherent in this calculation, it does not require, unlike the external field case, the determination of the plasma response to the perturbation, which was recently shown to have a significant impact on the NTV torque [56].

3.2. Formulation

MAST plasmas are mainly in the so-called $1/\nu$ collisionality regime (figure 8), where the particles trapped in banana orbits are collisionless and dominate the radial flux of ions. This regime is characterised by $q\omega_{E\times B} < \nu_{ii}/\epsilon < \sqrt{\epsilon}\omega_{t,i}$ with $\omega_{E\times B}$ the $E \times B$ drift frequency, ν_{ii} the thermal ion collision frequency, and ϵ the local aspect ratio. $\omega_{t,i} = (R_0 q)^{-1} v_{th,i}$ is the ion transit frequency, $v_{th,i}$ the thermal ion velocity and R_0 the major radius of the plasma.

The NTV theory is expressed in straight field line, constant Jacobian, Hamada coordinates (v, ζ, θ) [57], with v the volume enclosed by the flux surface, ζ and θ the toroidal and poloidal coordinates. From the usual geometrical flux coordinates (ψ, ϕ, θ_g) (ψ being the poloidal flux, ϕ and θ_g the geometrical toroidal and poloidal angles), they can be obtained by the transformation [58]:

$$v(\psi) = 2\pi \int_0^{\psi} \psi' \oint \frac{d\theta'_g}{\boldsymbol{B} \cdot \nabla\theta'_g} \tag{2a}$$

$$\zeta(\psi, \phi, \theta_g) = \frac{\phi}{2\pi} + F(\psi) \int_0^{\theta_g} \left(\left\langle \frac{1}{R^2} \right\rangle - \frac{1}{R^2} \right) \frac{d\theta'_g}{\boldsymbol{B} \cdot \nabla\theta'_g} \tag{2b}$$

$$\theta(\psi, \theta_g) = \left(\oint \frac{d\theta'_g}{\boldsymbol{B} \cdot \nabla\theta'_g} \right)^{-1} \left(\int_0^{\theta_g} \frac{d\theta'_g}{\boldsymbol{B} \cdot \nabla\theta'_g} \right) \tag{2c}$$

Note that with the conventions chosen here, ζ and θ are periodic, of period unity (not 2π). In equation 2*b*, $F(\psi) = RB_\phi$ with B_ϕ the toroidal field. Angled brackets denote a flux surface average carried out in the following manner:

$$\langle X \rangle = \left(\oint \frac{d\theta'_g}{\boldsymbol{B} \cdot \nabla\theta'_g} \right)^{-1} \left(\oint X \frac{d\theta'_g}{\boldsymbol{B} \cdot \nabla\theta'_g} \right) \tag{3}$$

Reference [58] details some properties of the coordinates built using equations 2*a*-2*c* but does not demonstrate that they are the Hamada coordinates. This is done in Appendix A. The braking depends on $|\boldsymbol{B}|$, the modulus of the total magnetic field, which needs

to be written in its Lagrangian form:

$$|\boldsymbol{B}(\boldsymbol{X}+\xi)| = |\boldsymbol{B}_0 + \delta\boldsymbol{B} + (\xi\cdot\nabla)\boldsymbol{B}| = |\boldsymbol{B}_0|\left(1+\sum_{(m,n)\neq(0,0)}\left(\frac{b_{n,m}}{|\boldsymbol{B}_0|}\right)e^{2\pi i(m\theta-n\zeta)}\right) \tag{4}$$

Here, $\boldsymbol{X}$, ξ and $\boldsymbol{B}_0$ are the position vector, the displacement vector, and the equilibrium magnetic field respectively. By construction, $b_{n,m}$ are the coefficients of the Fourier decomposition of the magnetic perturbation. In equation 4, the term $(\xi\cdot\nabla)\boldsymbol{B}$ is most easily calculated by exploiting the equilibrium field's axisymmetry and rewriting it as $(\xi\cdot\nabla)\boldsymbol{B} = \boldsymbol{B}_0(\boldsymbol{X}+\xi) - \boldsymbol{B}_0(\boldsymbol{X}) + O\left(|\xi|^2\right)$. This calculation is detailed in Appendix B and avoids tedious use of the tractable, though often diverging, $\nabla\times(\xi\times\boldsymbol{B})$ and $\nabla(\xi\cdot\boldsymbol{B})$ operators.

Rather than the expression given in [43], it is convenient to use the expression for the $1/\nu$ regime NTV torque given in [50], which makes use of the force balance equation for the ion fluid in order to express the torque as a function of the plasma profiles:

$$t_{\phi,NTV} = K\sum_{(m,n)\neq(0,0)}|nb_{m,n}|^2 W_{m,n} \qquad ((\omega_\phi-\omega^*_{NC})-\omega_{MHD}) \tag{5}$$

with:

$$K = 1.74 n_e \frac{eT_i}{2\nu_{ii}} R B_\phi \epsilon^{3/2}\langle R\rangle\left\langle B_\phi^{-1}\right\rangle\left\langle R^{-2}\right\rangle \tag{6}$$

Here, T_i, B_ϕ, R and ω_ϕ are the ion fluid temperature, the toroidal magnetic field, the major radius and the toroidal angular frequency respectively. The ion temperature and velocity are assumed to be equal to those of the carbon fluid measured by CXRS. ω_{MHD} is the angular frequency of the MHD, calculated by Fourier transform of the SXR signal, it accounts for the needed change from the lab frame to that of the MHD mode. The $W_{m,n}$ coefficients are given by:

$$W_{m,n} = \int_0^1 \frac{(F_{mnc}(\kappa))^2 + (F_{mns}(\kappa))^2}{E(\kappa)-(1-\kappa^2)K(\kappa)}d\kappa^2 \tag{7}$$

where κ is a pitch angle parameter defined in [43], $E(\kappa)$ and $K(\kappa)$ the complete elliptic of first and second kind. $F_{mnc}(\kappa)$ and $F_{mns}(\kappa)$ are defined by:

$$F_{mnc}(\kappa) = 2\int_0^{2Arcsin(\kappa)}\sqrt{\kappa^2 - sin^2(\theta/2)}\,cos((m-nq)\theta)d\theta \tag{8a}$$

$$F_{mns}(\kappa) = 2\int_0^{2Arcsin(\kappa)}\sqrt{\kappa^2 - sin^2(\theta/2)}\,sin((m-nq)\theta)d\theta \tag{8b}$$

ω^*_{NC} is a neoclassical offset angular frequency defined as:

$$\omega^*_{NC} = \frac{3.5}{Ze\bar{R}B_p}\left(\frac{dT_i}{dr}\right) \tag{9}$$

where B_p and r are the poloidal field and minor radius. $\bar{R}$ is the major radius of outboard mid-plane point of the flux surface. This offset rotation has been shown to be of importance [59].

The NTV torque given by equation 5 is proportional to the squared amplitude of the magnetic perturbation, and to the difference of the ion fluid and mode's frequencies, $\omega_\phi - \omega_{MHD}$ (with an additional offset ω^*_{NC}), as expected from the heuristic mechanisms introduced in section 3.1.

4. MAST results

The comparison described in the previous sections and summarised in figure 2 was carried out on MAST plasmas featuring the LLM, a saturated ideal MHD mode. The eigenstructure calculated by CASTOR, for an equilibrium reconstructed at the LLM appearance, is an $n = 1$ internal kink mode, shown in figure 9. The best agreement between SXR simulations and experimental data is obtained for a radial amplitude $\xi_r = 1.2$cm. The relative amplitudes as well as the phases of the SXR fluctuations are well matched for each channel (figures 10 and 11). This best match corresponds to a clear local minimum of the simulation's residuals with respect to the measured data (figure 12), which gives good confidence in the estimated amplitude. As mentioned in section 2, no π phase jumps are observed in the SXR fluctuations, tending to rule out electromagnetic torques associated with magnetic reconnection.

The rotation frequency profiles of the plasma during the braking are shown in figure 13. The rotation is unchanged for the radial location $R = 1.15$m. It is tempting to interpret this point as the position where the mode's frequency and that of the plasma are equal, hence where one would expect the torque applied by the mode to vanish. This is actually not the case, and the dashed line in figure 13 indicates the frequency of the mode at its onset. Although it decreases on equilibrium timescales, this latter frequency does not reach that of the plasma at $R = 1.15$m at any time. This gap between the rotation frequency of the plasma at $R = 1.15$m and that of the mode can be explained by the presence of the offset frequency ω^*_{NC} in the NTV formulation (equation 5), and these two shifts are of similar magnitude.

When the LLM appears, the plasma is assumed in a steady state from the point of view of angular momentum transport. This means that the angular momentum input from NBI exactly balances momentum transport and losses. The braking of the plasma takes place on time scales faster than the momentum confinement time ($\sim$ 50ms on MAST), such the that NBI source can still be assumed to balance the momentum transport and losses during the first milliseconds of the braking: over this period, the latter is solely due to MHD. The comparison carried out in this study focuses on this early rotation damping. Analysing later time slices would require an additional assumption on the transport of angular momentum, which cannot confidently be made. Note however that the LLM increases fast ion losses, possibly leading to two phenomena neglected here: the torque deposition may be slightly altered after mode onset and the fast ion redistribution is likely to affect plasma rotation. Initial calculations of this second effect however indicate that it is significantly lower than the observed damping. More accurate calculations using the HAGIS drift kinetic code are to be carried out in the future.

The torque predicted by NTV at $t = 255$ms is plotted in figure 14, together with the measured rate of change of angular momentum for each flux tube. The predictions and observations have the same order of magnitude. The profile shapes are similar, except in the vicinity of the rational surfaces and the inertial layer, the latter being

located at the q_{min} surface, due to the absence of a $q = 1$ surface. In these regions, large parallel magnetic field perturbations result in a high torque which is not observed in the experimental data. Since the linear structure used here only differs from the non-linear saturated one at these positions [34, 49], this disagreement is not regarded as invalidating the applicability of the theory to the observations. The uncertainties in the different plasma profiles involved in the calculation are bounded at a level that does not compromise the calculated order of magnitude of the results, nor the shape of the profile. Nevertheless, they do not allow more detailed comparisons, and seem not accurate enough to have a predictive use. It is however worth mentioning that the inclusion of the offset frequency ω^*_{NC} is crucial in order to reproduce the measured torque profile with NTV theory. Furthermore, the Lagrangian term $(\xi \cdot \nabla)\, \boldsymbol{B}$ must be taken into account to predict a torque of magnitude comparable to the one observed experimentally, neglecting it decreases the calculated result by up to 70%, especially in the vicinity of the magnetic axis.

5. Conclusions

MAST NBI-heated plasmas with low density exhibit a weakly reversed shear q profile just above 1, prone to the appearance of the LLM, a saturated long-lived MHD instability. All experimental observations indicate that the mode is ideal in nature, which is corroborated by analytical work and modelling [37, 38]. Measurements show strong core damping of the sheared toroidal rotation simultaneous to the mode onset. The eigenstructure of the mode was calculated using the CASTOR code, and its saturated amplitude determined using the fluctuations of SXR experimental data. The structure of the magnetic perturbation obtained was used to estimate the braking torque induced by the mode according to NTV theory, the rationale of this entire study being summarised in figure 2. The results were found in agreement with the experiment, in terms of order of magnitude and profile.

In previous work, NTV has mainly been applied to externally applied magnetic perturbations [54,55]. The similarity between predictions and experimental observations are encouragements that this theory is also a good candidate mechanism for the interaction between MHD and plasma rotation, as described in section 3. For this type of study, the theory is applied in the frame moving with the MHD mode, which has a rigid body rotation. This application to an MHD instability also provides an additional observation of the offset rotation term ω^*_{NC}, after that made in experiments with coil-induced magnetic perturbations on DIII-D [59].

The present study of the interplay between an MHD mode and rotation is not limited to MAST cases, but is relevant to several tokamaks exploiting scenarios with hybrid-like, reversed shear q profiles just above an integer value. Ideal saturated $(m, n) = (2, 1)$ modes are observed in JET's hybrid plasmas with $q_{min} > 2$ [60, 61]. This so-called continuous mode also results in a flattening of core rotation. Slowly growing ideal modes associated with hybrid like q profile and high normalised pressure have also been observed on DIII-D [62] and JT-60U [63], with a simultaneous collapse of the toroidal rotation. Damping of core rotation by MHD has also been observed in NSTX [64], although the mode was observed to be resistive and the braking attributed to electromagnetic torques arising from magnetic reconnection.

Appendix A. Hamada coordinates

The Hamada coordinates (v, ζ, θ) [57] have the following properties:

Property 1 *The first coordinate is the volume enclosed by the flux surfaces.*

Property 2 *They are straight field line coordinates, meaning that* $(\boldsymbol{B} \cdot \nabla\zeta)(\boldsymbol{B} \cdot \nabla\theta)^{-1} = q(v)$ *and this ratio is equal to the usual safety factor, which in usual geometrical flux coordinates is* $q(v) = (2\pi)^{-1} \oint (\boldsymbol{B} \cdot \nabla\phi)(\boldsymbol{B} \cdot \nabla\theta_g)^{-1} d\theta_g$.

Property 3 *All the contravariant components of the magnetic field are flux functions.*

Property 4 *Their Jacobian is constant and unity.*

These properties uniquely define the Hamada covariant basis, hence the full coordinates, since: ∇v is fully determined by property 1, properties 2 and 3 set the relative angles and magnitudes of $\nabla\zeta$ and $\nabla\theta$, and lastly, property 4 sets the relative angles and magnitudes of ∇v on the one hand and $(\nabla\zeta, \nabla\theta)$ on the other hand. It is shown in this section that the coordinates (v, ζ, θ), given by equations $2a$-$2c$, satisfy these four properties and therefore are the Hamada coordinates.

It should first be mentioned that the integral $\oint X \left(\boldsymbol{B} \cdot \nabla\theta'_g\right)^{-1} d\theta'_g$ is left unchanged by any monotonic periodic variable change:

$$\theta'_g = (\eta) \Rightarrow \begin{cases} d\theta'_g = f'(\eta)\, d\eta \\ \nabla\theta'_g = f'(\eta)\, \nabla\eta \end{cases} \Rightarrow \oint X \frac{d\theta'_g}{\boldsymbol{B} \cdot \nabla\theta'_g} = \oint X \frac{d\eta}{\boldsymbol{B} \cdot \nabla\eta} \tag{A.1}$$

While not directly relevant to this demonstration, this property interestingly shows that any monotonic periodic poloidal coordinate can be used in place of θ_g to build the (v, ζ, θ) coordinates.

Property 1 is a simple matter of definition. To prove the validity of properties 2-4, it is useful to note a few points beforehand. To begin with, the definition of the volume in equation $2a$ comes from the basic properties of the magnetic field, allowing one to express it as $\boldsymbol{B} = F(\psi)\nabla\phi + \nabla\psi \times \nabla\phi$. Since $\nabla\theta_g \cdot \nabla\phi = 0$, this gives:

$$dV = \frac{d\psi\, d\phi\, d\theta_g}{\nabla\psi \cdot (\nabla\phi \times \nabla\theta_g)} \tag{A.2}$$

$$= \frac{d\psi\, d\phi\, d\theta_g}{\nabla\theta_g \cdot (\nabla\psi \times \nabla\phi)} \tag{A.3}$$

$$= \frac{d\psi\, d\phi\, d\theta_g}{\boldsymbol{B} \cdot \nabla\theta_g} \tag{A.4}$$

and therefore:

$$v(\psi) = 2\pi \int_0^\psi d\psi' \oint \frac{d\theta'_g}{\boldsymbol{B} \cdot \nabla\theta'_g} \tag{A.5}$$

In addition, the third covariant vector of the (v, ζ, θ) coordinates is:

$$\nabla\theta = \frac{\partial\theta}{\partial\psi}\nabla\psi + \frac{\partial\theta}{\partial\theta_g}\nabla\theta_g \tag{A.6}$$

$$= \frac{\partial\theta}{\partial\psi}\nabla\psi + \left(\oint \frac{d\theta_g}{\boldsymbol{B} \cdot \nabla\theta_g}\right)^{-1} \frac{\nabla\theta_g}{\boldsymbol{B} \cdot \nabla\theta_g} \tag{A.7}$$

Hence:

$$\boldsymbol{B}\cdot\nabla\theta = \frac{\partial\theta}{\partial\psi}\boldsymbol{B}\cdot\nabla\psi + \left(\oint\frac{d\theta_g}{\boldsymbol{B}\cdot\nabla\theta_g}\right)^{-1}\frac{\boldsymbol{B}\cdot\nabla\theta_g}{\boldsymbol{B}\cdot\nabla\theta_g} \tag{A.8}$$

$$= \left(\oint\frac{d\theta_g}{\boldsymbol{B}\cdot\nabla\theta_g}\right)^{-1} \tag{A.9}$$

Note that this equation also shows that $\boldsymbol{B}\cdot\nabla\theta$ is a derivative of the volume. Additionally, it follows from equation A.6 that:

$$\boldsymbol{B}\cdot\nabla\theta = \frac{\partial\theta}{\partial\theta_g}\boldsymbol{B}\cdot\nabla\theta_g \tag{A.10}$$

This means successively:

$$\frac{\nabla\theta_g}{\boldsymbol{B}\cdot\nabla\theta_g} = \frac{\nabla\theta}{\boldsymbol{B}\cdot\nabla\theta} + \frac{\partial\theta_g}{\partial\psi}\frac{\nabla\psi}{\boldsymbol{B}\cdot\nabla\theta_g} \tag{A.11}$$

$$\frac{\nabla\psi\times\nabla\theta_g}{\boldsymbol{B}\cdot\nabla\theta_g} = \frac{\nabla\psi\times\nabla\theta}{\boldsymbol{B}\cdot\nabla\theta} \tag{A.12}$$

Lastly, the covariant vectors of the (v,ζ,θ) coordinates are given by simple differentiation, and use of equation A.9:

$$\nabla v = \frac{2\pi}{\boldsymbol{B}\cdot\nabla\theta}\nabla\psi \tag{A.13}$$

$$\nabla\zeta = \frac{\partial\zeta}{\partial\psi}\nabla\psi + \frac{1}{2\pi}\nabla\phi + \frac{F(\psi)}{2\pi}\left(\left\langle\frac{1}{R^2}\right\rangle - \frac{1}{R^2}\right)\frac{\nabla\theta_g}{\boldsymbol{B}\cdot\theta_g} \tag{A.14}$$

$$\nabla\theta = \frac{\partial\theta}{\partial\psi}\nabla\psi + \boldsymbol{B}\cdot\nabla\theta\frac{\nabla\theta_g}{\boldsymbol{B}\cdot\nabla\theta_g} \tag{A.15}$$

With these remarks in mind, it is possible to easily prove properties 2 to 4.

By definition, $\boldsymbol{B}\cdot\nabla v = 0$, and equation A.9 indicates that $\boldsymbol{B}\cdot\nabla\theta$ is a flux function. Taking the scalar product of $\boldsymbol{B}$ with equation A.14 results in:

$$\boldsymbol{B}\cdot\nabla\zeta = \frac{1}{2\pi}\boldsymbol{B}\cdot\nabla\phi + \frac{F(\psi)}{2\pi}\frac{\boldsymbol{B}\cdot\nabla\theta_g}{\boldsymbol{B}\cdot\nabla\theta_g}\left(\left\langle\frac{1}{R^2}\right\rangle - \frac{1}{R^2}\right) \tag{A.16}$$

Since by definition of $F(\psi)$ and ϕ, $\boldsymbol{B}\cdot\nabla\phi = F(\psi)R^{-2}$, we have:

$$\boldsymbol{B}\cdot\nabla\zeta = \frac{F(\psi)}{2\pi}\left\langle\frac{1}{R^2}\right\rangle \tag{A.17}$$

This equation guarantees that $\boldsymbol{B}\cdot\nabla\zeta$ is the flux surface average of $\boldsymbol{B}\cdot\nabla\phi$. Consequently, all contravariant components of the magnetic field are flux functions and property 3 is verified.

Substituting for $\boldsymbol{B}\cdot\nabla\phi = R^{-2}F(\psi)$ in the safety factor definition gives:

$$q(v) = \frac{1}{2\pi}\oint\frac{F(\psi)/(2\pi R^2)}{\boldsymbol{B}\cdot\nabla\theta_g}d\theta_g \tag{A.18}$$

$$= \frac{F(\psi)}{2\pi}\oint\frac{d\theta_g/R^2}{\boldsymbol{B}\cdot\nabla\theta_g} \tag{A.19}$$

Now using the the definition of the flux surface average (equation 3) together with equations A.17 and A.9:

$$q\left(v\right) = \left(\oint \frac{d\theta_g}{\boldsymbol{B}\cdot\nabla\theta_g}\right)\boldsymbol{B}\cdot\nabla\zeta \tag{A.20}$$

$$= \frac{\boldsymbol{B}\cdot\nabla\zeta}{\boldsymbol{B}\cdot\nabla\theta} \tag{A.21}$$

This demonstrates that property 2 is verified.

There only remains to prove property 4. This is done by calculating the Jacobian of the coordinates (v,ζ,θ). Taking the cross-product of equations A.13 and A.14 gives:

$$\nabla v\times\nabla\zeta = \frac{1}{\boldsymbol{B}\cdot\nabla\theta}\left(\nabla\psi\times\nabla\phi + F\left(\psi\right)\left(\left\langle\frac{1}{R^2}\right\rangle - \frac{1}{R^2}\right)\frac{\nabla\psi\times\nabla\theta_g}{\boldsymbol{B}\cdot\nabla\theta_g}\right) \tag{A.22}$$

Using equation A.12 to transform the second term on the right hand side:

$$\nabla v\times\nabla\zeta = \frac{1}{\boldsymbol{B}\cdot\nabla\theta}\left(\nabla\psi\times\nabla\phi + F\left(\psi\right)\left(\left\langle\frac{1}{R^2}\right\rangle - \frac{1}{R^2}\right)\frac{\nabla\psi\times\nabla\theta}{\boldsymbol{B}\cdot\nabla\theta}\right) \tag{A.23}$$

Taking the scalar product of equations A.23 with $\nabla\theta$, the second term on the right hand side vanishes leaving:

$$\left(\nabla v\times\nabla\zeta\right)\cdot\nabla\theta = \frac{1}{\boldsymbol{B}\cdot\nabla\theta}\left(\left(\nabla\psi\times\nabla\phi\right)\cdot\nabla\theta\right) \tag{A.24}$$

Substituting for $\nabla\theta$ on the right hand side using equation A.15 then yields:

$$\left(\nabla v\times\nabla\zeta\right)\cdot\nabla\theta = \frac{1}{\boldsymbol{B}\cdot\nabla\theta}\left(\left(\nabla\psi\times\nabla\phi\right)\left(\frac{\partial\theta}{\partial\psi}\nabla\psi + \boldsymbol{B}\cdot\nabla\theta\frac{\nabla\theta_g}{\boldsymbol{B}\cdot\nabla\theta_g}\right)\right) \tag{A.25}$$

$$= \left(\nabla\psi\times\nabla\phi\right)\cdot\frac{\nabla\theta_g}{\boldsymbol{B}\cdot\nabla\theta_g} \tag{A.26}$$

Using equations A.4 and A.26 eventually proves property 4:

$$\left(\nabla v\times\nabla\zeta\right)\cdot\nabla\theta = \frac{\left(\nabla\psi\times\nabla\phi\right)\cdot\nabla\theta_g}{\boldsymbol{B}\cdot\nabla\theta_g} \tag{A.27}$$

$$= \frac{\boldsymbol{B}\cdot\nabla\theta_g}{\boldsymbol{B}\cdot\nabla\theta_g} \tag{A.28}$$

$$= 1 \tag{A.29}$$

The (v,ζ,θ) coordinates built using equations 2*a*-2*c* therefore verify properties 1-4, and thus are the Hamada coordinates. Their construction is closely linked to the expression of the volume given by equation A.4 and the flux surface average defined in equation 3.

Appendix B. Calculation of $(\xi \cdot \nabla)\boldsymbol{B}$

NTV theory requires the magnetic perturbation to be expressed in the Lagrangian form. The Lagrangian term to be added to the Eulerian form of $\delta\boldsymbol{B}$ is simply the contribution of the displacement of the fluid cell to the perturbation, $(\xi \cdot \nabla)\boldsymbol{B} = \boldsymbol{B}_0(\boldsymbol{X}+\xi) - \boldsymbol{B}_0(\boldsymbol{X}) + O\left(|\xi|^2\right)$. To carry out this calculation, the equilibrium magnetic field is most conveniently decomposed on the usual cylindrical local basis $(\boldsymbol{e}_R, \boldsymbol{e}_\phi, \boldsymbol{e}_Z)$, but with the use of the (ψ, ϕ, θ_g) coordinates to locate a point in space:

$$\boldsymbol{B}_0(\boldsymbol{X}) = B_{0,R}(\psi,\theta_g)\,\boldsymbol{e}_R + B_{0,\phi}(\psi,\theta_g)\,\boldsymbol{e}_\phi + B_{0,Z}(\psi,\theta_g)\,\boldsymbol{e}_Z \tag{B.1}$$

According to basic differential geometry, the equilibrium field at $\boldsymbol{X}+\xi$ is:

$$\boldsymbol{B}_0(\boldsymbol{X}+\xi) = \boldsymbol{B}_0(\boldsymbol{X}) + \frac{\partial \boldsymbol{B}_0}{\partial\psi}(\nabla\psi\cdot\xi) + \frac{\partial \boldsymbol{B}_0}{\partial\phi}(\nabla\phi\cdot\xi) + \frac{\partial \boldsymbol{B}_0}{\partial\theta_g}(\nabla\theta_g\cdot\xi) + O\left(|\xi|^2\right) \tag{B.2}$$

Therefore:

$$(\xi\cdot\nabla)\boldsymbol{B} = \frac{\partial \boldsymbol{B}_0}{\partial\psi}\xi^\psi + \frac{\partial \boldsymbol{B}_0}{\partial\phi}\xi^\phi + \frac{\partial \boldsymbol{B}_0}{\partial\theta_g}\xi^{\theta_g} + O\left(|\xi|^2\right) \tag{B.3}$$

The differential forms of $\boldsymbol{B}_0$ must be calculated taking into account that the field is axisymmetric and that the chosen basis vectors are not constant in space but depend on the toroidal angle. This gives, for $\alpha \in (\psi, \theta_g)$:

$$\frac{\partial \boldsymbol{B}_0}{\partial\alpha} = \frac{\partial B_{0,R}}{\partial\alpha}\boldsymbol{e}_R + \frac{\partial B_{0,\phi}}{\partial\alpha}\boldsymbol{e}_\phi + \frac{\partial B_{0,Z}}{\partial\alpha}\boldsymbol{e}_Z \tag{B.4}$$

and:

$$\frac{\partial \boldsymbol{B}_0}{\partial\phi} = B_{0,R}\frac{\partial \boldsymbol{e}_R}{\partial\phi} + B_{0,\phi}\frac{\partial \boldsymbol{e}_\phi}{\partial\phi} + B_{0,Z}\frac{\partial \boldsymbol{e}_Z}{\partial\phi} = B_{0,R}\boldsymbol{e}_\phi - B_{0,\phi}\boldsymbol{e}_R \tag{B.5}$$

Equations B.3, B.4, B.5 allow a simple calculation of the Lagrangian term of the magnetic perturbation, avoiding the intricate, although widespread, use of the $\nabla\times(\xi\times\boldsymbol{B})$ and $\nabla(\xi\cdot\boldsymbol{B})$ operators. Each of these individually diverge, but their diverging parts cancel each other in the combination involved in $(\xi\cdot\nabla)\boldsymbol{B}$. The Lagragian term is given in its simple form by:

$$\begin{aligned}(\xi\cdot\nabla)\boldsymbol{B} = {}& \xi^\psi\left(\frac{\partial B_{0,R}}{\partial\psi}\boldsymbol{e}_R + \frac{\partial B_{0,\phi}}{\partial\psi}\boldsymbol{e}_\phi + \frac{\partial B_{0,Z}}{\partial\psi}\boldsymbol{e}_Z\right)\\ &+ \xi^\phi\left(\frac{\partial B_{0,R}}{\partial\theta_g}\boldsymbol{e}_R + \frac{\partial B_{0,\phi}}{\partial\theta_g}\boldsymbol{e}_\phi + \frac{\partial B_{0,Z}}{\partial\theta_g}\boldsymbol{e}_Z\right)\\ &+ \xi^{\theta_g}\left(B_{0,R}\boldsymbol{e}_\phi - B_{0,\phi}\boldsymbol{e}_R\right)\\ &+ O\left(|\xi|^2\right)\end{aligned} \tag{B.6}$$

Acknowledgments

The authors would like to acknowledge useful discussions with Dr N Arcis, Dr TC Hender, Dr CG Gimblett and Dr YQ Liu. This work was partly funded by the United Kingdom Engineering and Physical Sciences Research Council under grant EP/G003955, the Ecole Polytechnique (Palaiseau, France), the British Council and by the European Communities under the Contract of Association between EURATOM and CCFE. The views and opinions expressed herein do not necessarily reflect those of the European Commission.

References

[1] De Vries PC *et al.*, 2008 *Nucl. Fusion* **48** 065006
[2] Connor JW *et al.*, 2004 *Nucl. Fusion* **44** R1
[3] Roach C *et al.*, 2009 *36th EPS Conference on Plasma Physics, Sofia* I4.070
[4] Cooper WA 1988 *Plasma Phys. Control. Fusion* **30** 1805
[5] Miller R *et al.*, 1995 *Phys. Plasmas* **2** 3676
[6] Connor JW *et al.*, 2004 *Plasma Phys. Control. Fusion* **46** B1
[7] Furukawa M *et al.*, 2005 *Nucl. Fusion* **45** 377
[8] Wilson HR 1993 *Plasma Phys. Control. Fusion* **35** 885
[9] Wahlberg C *et al.*, 2000 *Phys. Plasmas* **7** 923
[10] Waelbroeck FL, 1996 *Phys. Plasmas* **3** 1047
[11] Chapman IT *et al.*, 2006 *Nucl. Fusion* **46** 1009
[12] Chapman IT *et al.*, 2008 *Nucl. Fusion* **48** 035004
[13] Chapman IT *et al.*, 2009 *Nucl. Fusion* **49** 035006
[14] Becoulet A *et al.*, 2008 *Plasma Phys. Control. Fusion* **50** 124055
[15] Litaudon X *et al.*, 2007 *Plasma Phys. Control. Fusion* **49** B529
[16] Joffrin E, 2007 *Plasma Phys. Control. Fusion* **49** B629
[17] Doyle EJ *et al.*, 2006 *Plasma Phys. Control. Fusion* **48** B39
[18] Taylor TS 1997 *Plasma Phys. Control. Fusion* **39** B47
[19] Bickerton RJ *et al.*, 1971 *Nat. Phys. Sci.* **229** 110
[20] Sips ACC *et al.*, 2005 *Plasma Phys. Control. Fusion* **47** A19
[21] Joffrin E, 2005 *Nucl. Fusion* **45** 626
[22] Bondeson A *et al.*, 1994 *Phys. Rev. Lett.* **72** 2709
[23] Gimblett CG 1986 *Nucl. Fusion* **26** 617
[24] Strait EJ *et al.*, 1995 *Phys. Rev. Lett.* **74** 2483
[25] Hender TC *et al.*, 2006 *21st IAEA Fusion Energy Conference, Chengdu, China* EX/P8-18
[26] Sabbagh SA *et al.*, 2006 *Nucl. Fusion* **46** 635
[27] Garofalo AM *et al.*, 2002 *Phys. Plasmas* **9** 1997
[28] La Haye RJ *et al.*, 2004 *Nucl. Fusion* **44** 1197
[29] Sontag AC *et al.*, 2005 *Phys. Plasmas* **12** 056112
[30] Fitzpatrick R *et al.*, 2003 *Phys. Plasmas* **10** 1782
[31] Saarelma S *et al.*, 2007 *Plasma Phys. Control. Fusion* **49** 31
[32] Nave MFF *et al.*, 1990 *Nucl. Fusion* **30** 2575
[33] Hastie RJ *et al.*, 1987 *Phys. Fluids* **30** 1756
[34] Avinash *et al.*, 1987 *Phys. Rev. Lett.* **59** 2647
[35] Wahlberg C *et al.*, 2007 Phys. Plasmas **14** 110703
[36] Manickam J *et al.*, 1987 Nucl. Fusion **27** 1461
[37] Hua M-D *et al.* 2009 *sub Plasma Phys. Control. Fusion*
[38] Chapman IT *et al.* 2009 *sub Nucl. Fusion*
[39] Pinches SD *et al.*, 1998 *Comput. Phys. Commun.* **111** 133
[40] Fitzpatrick R *et al.* 1993 *Nucl. Fusion* **33** 1533
[41] Gimblett CG *et al.*, 2000 Phys. Plasmas **7** 258
[42] Taylor JB *et al.*, 2003 *Phys. Rev. Lett.* **91** 115002
[43] Shaing KC, 2003 *Phys. Plasmas* **10** 1443
[44] Kerner W *et al.*, 1998 *J. Comp. Phys.* **142** 271
[45] Lao L *et al.*, 1990 *Nucl. Fusion* **30** 1035
[46] Huysmans G *et al.*, 1991 *Proceedings of the CP90 Conference on Computer Physics*, (World Scientific, Singapore), p. 371
[47] Fitzpatrick R, 1995 *Phys. Plasmas* **2** 825
[48] Hutchinson IH, 2002 *Principles of Plasma Diagnostics* 2nd ed. (Cambridge: Cambridge University

Press) p200
[49] Rosenbluth MN *et al.*, 1973 *Phys. Fluids* **16** 1894
[50] Cole AJ *et al.*, 2007 *Phys. Rev. Lett.* **99** 065001
[51] Hassam AB *et al.*, 1978 *Phys. Fluids* **21** 2271
[52] Hirshman SP *et al.*, 1981 *Nucl. Fusion* **9** 1079
[53] Shaing KC *et al.*, 1983 *Phys. Fluids* **26** 3315
[54] Zhu W *et al.*, 2006 *Phys. Rev. Lett.* **96** 225002
[55] Garofalo AM *et al.*, 2008 *Phys. Rev. Lett.* **101** 195005
[56] Park J-K *et al.*, 2009 *Phys. Plasmas* **16** 056115
[57] Hamada S, 1962 *Nucl. Fusion* **2** 23
[58] Scott BD, `www.ipp.mpg.de/~bds/write-ups/hamada/coords.ps`
[59] Garofalo AM *et al.*, 2009 *Phys. Plasmas* **16** 056119
[60] Buratti P *et al.*, 2008 *35th EPS Conference on Plasma Physics, Hersonissos* P1.069
[61] Buratti P *et al.*, 2009 *36th EPS Conference on Plasma Physics, Sofia* O2.007
[62] Okabayashi M *et al.*, 2008 *22nd IAEA Fusion Energy Conference, Geneva* EX/P9-5
[63] Matsunaga G *et al.*, 2008 *22nd IAEA Fusion Energy Conference, Geneva* EX/5-2
[64] Menard JE *et al.*, 2005 *Nucl. Fusion* **45** 539

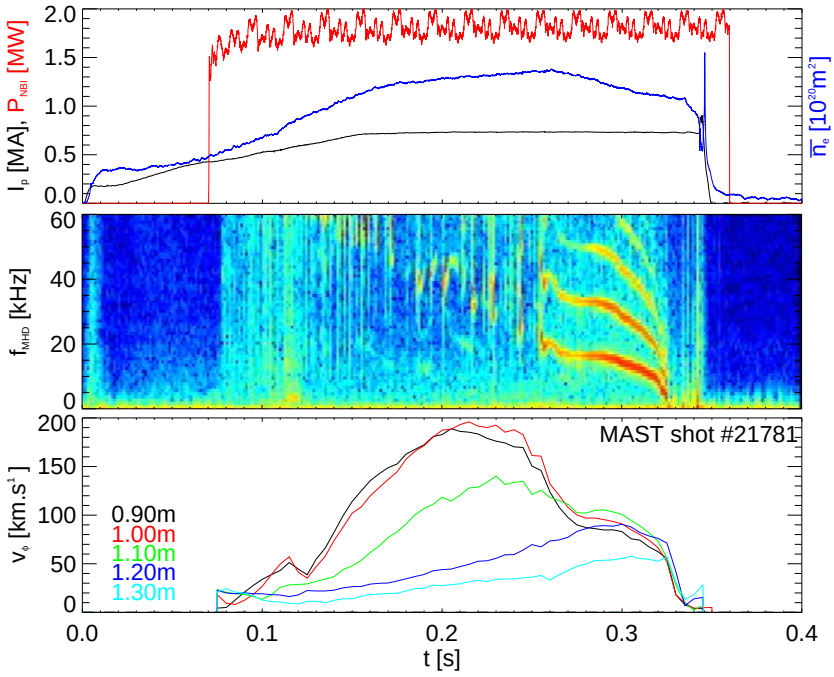

Figure 1. Top: plasma current, auxiliary heating power and line-integrated density. Middle: spectrogram of the mode from the outboard Mirnov coils. Bottom: Toroidal rotation measured by CXRS at different radial locations of the plasma, showing the damping of core rotation concurrent with the MHD mode onset. The magnetic axis is located at $R = 0.95$m and the outboard edge at $R = 1.40$m.

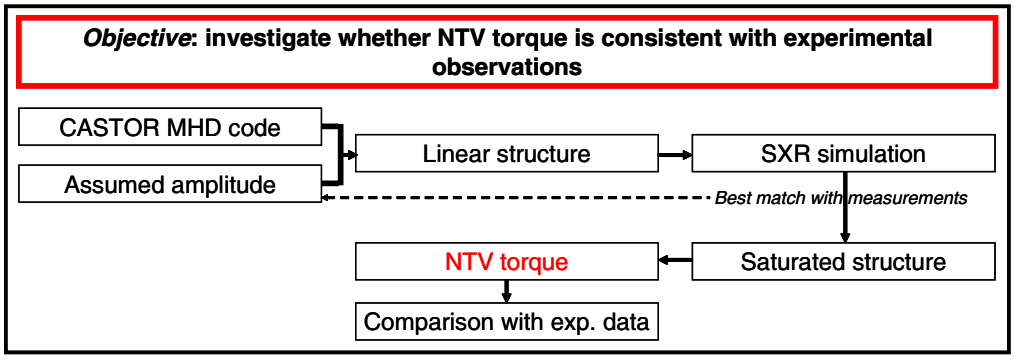

Figure 2. Rationale of the theory-experiment comparison carried out in this study.

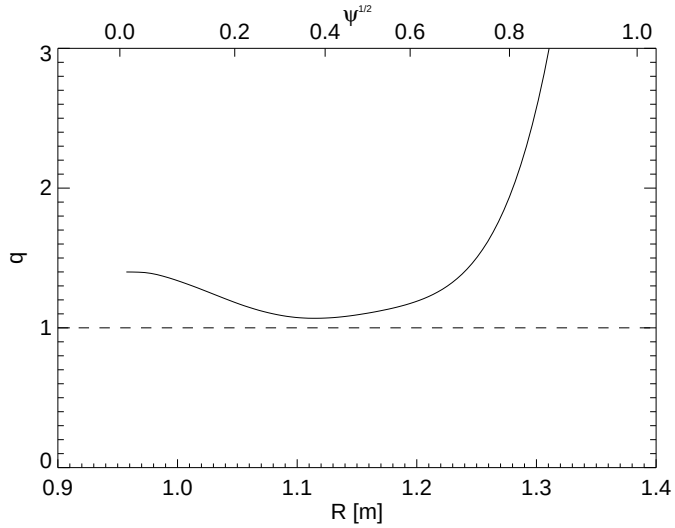

Figure 3. q profile for MAST shot 21508 at mode onset (255ms), calculated by EFIT constrained to magnetic field pitch-angle data from MSE and total pressure data from TS and CXRS.

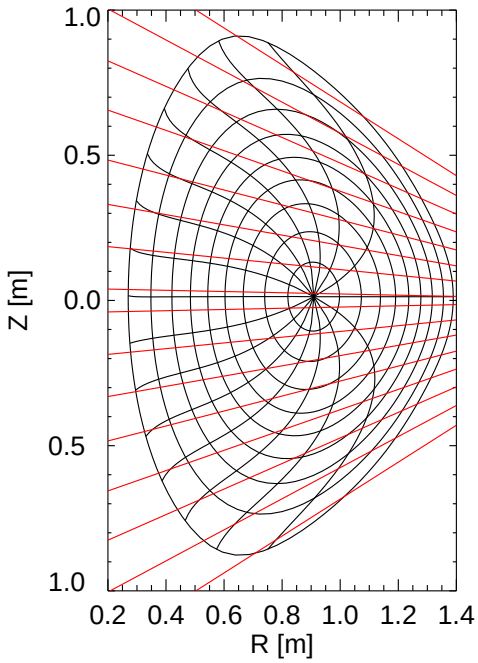

Figure 4. Poloidal cross-section of a MAST plasma showing the lines of sight of the horizontal SXR array. The nested contours are flux surfaces with normalised poloidal flux lower than 0.95, the curves converging towards the magnetic axis represent lines of constant poloidal coordinates used in the HELENA and CASTOR codes.

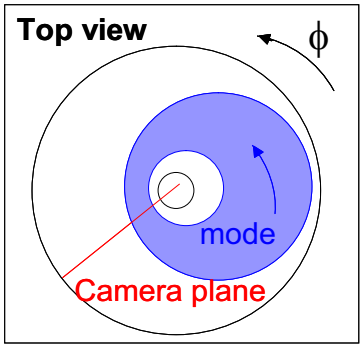

Figure 5. Top view of MAST showing the horizontal SXR array position and a schematic of an MHD mode moving past the SXR lines of sight.

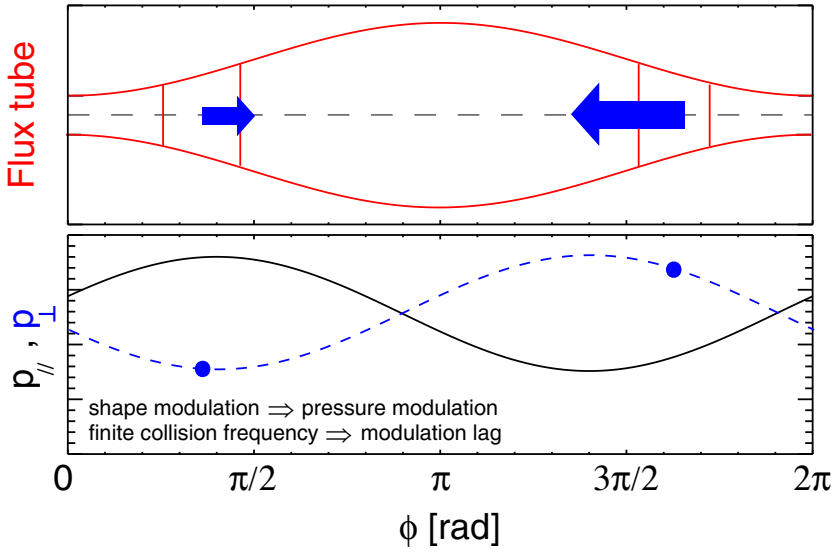

Figure 6. Heuristic mechanism of magnetic pumping. The top panel represents a distorted flux tube cut open and straightened. The bottom panel shows the modulation of the parallel (plain line) and perpendicular (dashed line) pressures caused by the shape modulation. The effect of collisions not being instantaneous, the modulation of pressures lag that of shape. As the fluid cell moves toroidally, the work of the perpendicular pressure during the first half of the cycle, which is in the direction of the motion, (left) is less than that during the second half of the cycle, which opposes the motion (right). Estimating the work of parallel pressure is more difficult since it needs to take into account the pressure gradient, the variation of the cross section and the length of the fluid element. Nevertheless, it also opposes the motion.

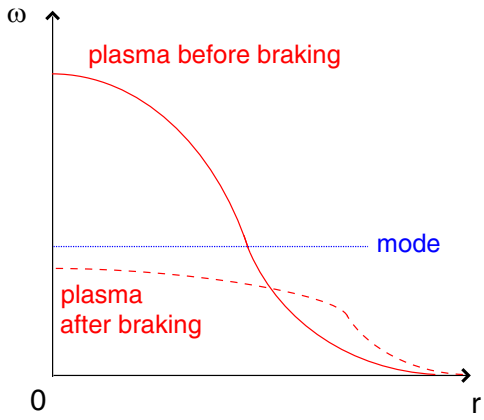

Figure 7. The two competing angular frequency profiles in a rotating plasma with an MHD mode: that of the plasma (plain line) and that of the mode (dotted line). These profiles are brought in agreement by the damping of the plasma rotation, with a departure of the plasma angular frequency from that of the MHD of order the diamagnetic frequency, ω^*_{NC} (dashed line). This process is described by equation 5.

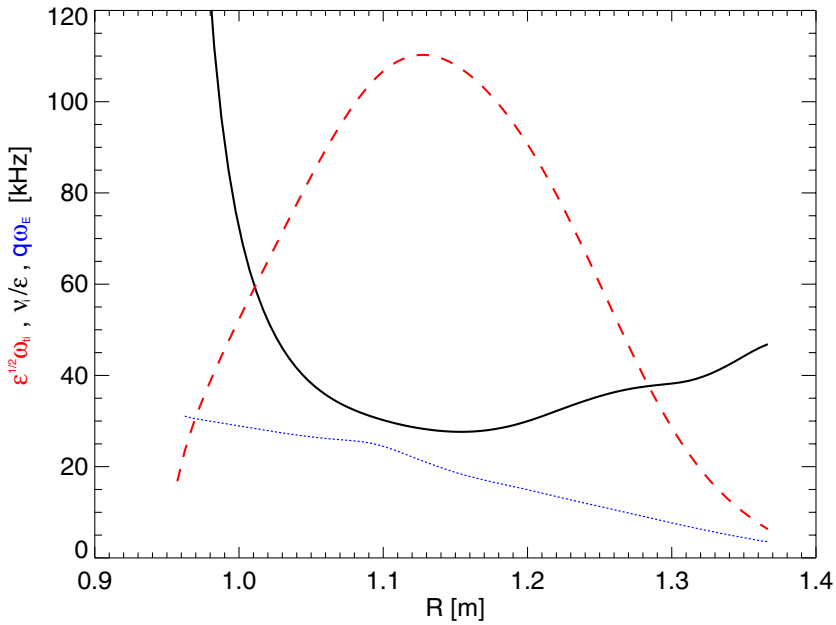

Figure 8. Validity of the $1/\nu$ regime for MAST shot 21508 at $t = 255$ms. This regime is characterised by $q\omega_{E\times B} < \nu_i/\epsilon < \sqrt{\epsilon}\omega_{t,i}$, where $q\omega_{E\times B}$ is represented by the dotted line, ν_i/ϵ by the solid line, and $\sqrt{\epsilon}\omega_{t,i}$ by the dashed line.

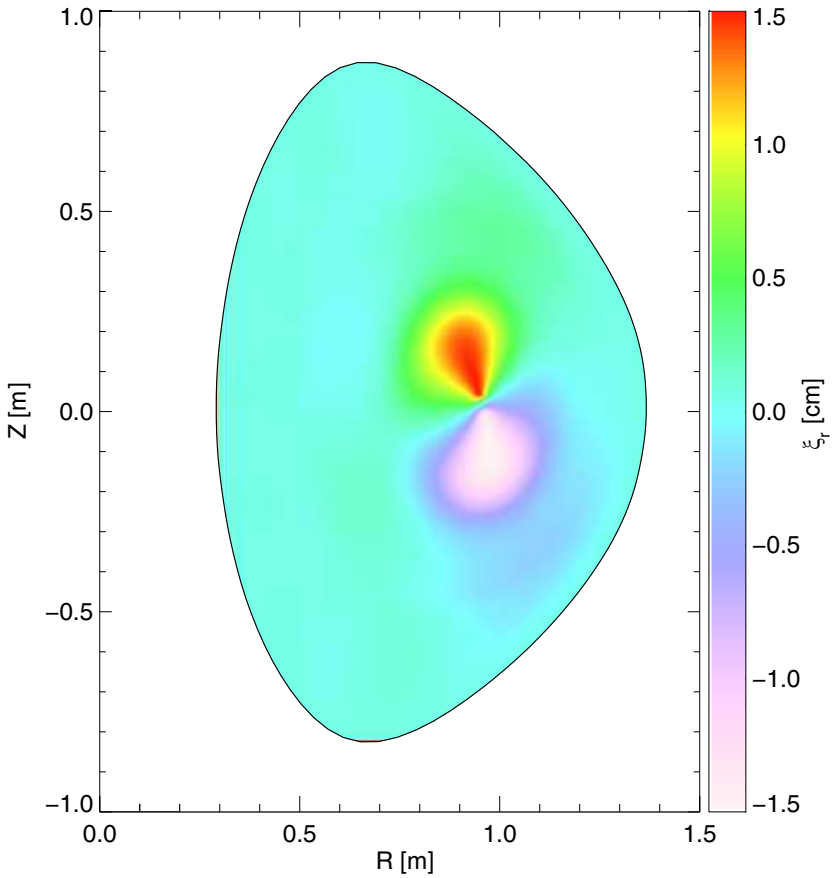

Figure 9. The radial displacement in centimetres calculated by the CASTOR code for MAST shot 21508 at $t = 255$ms.

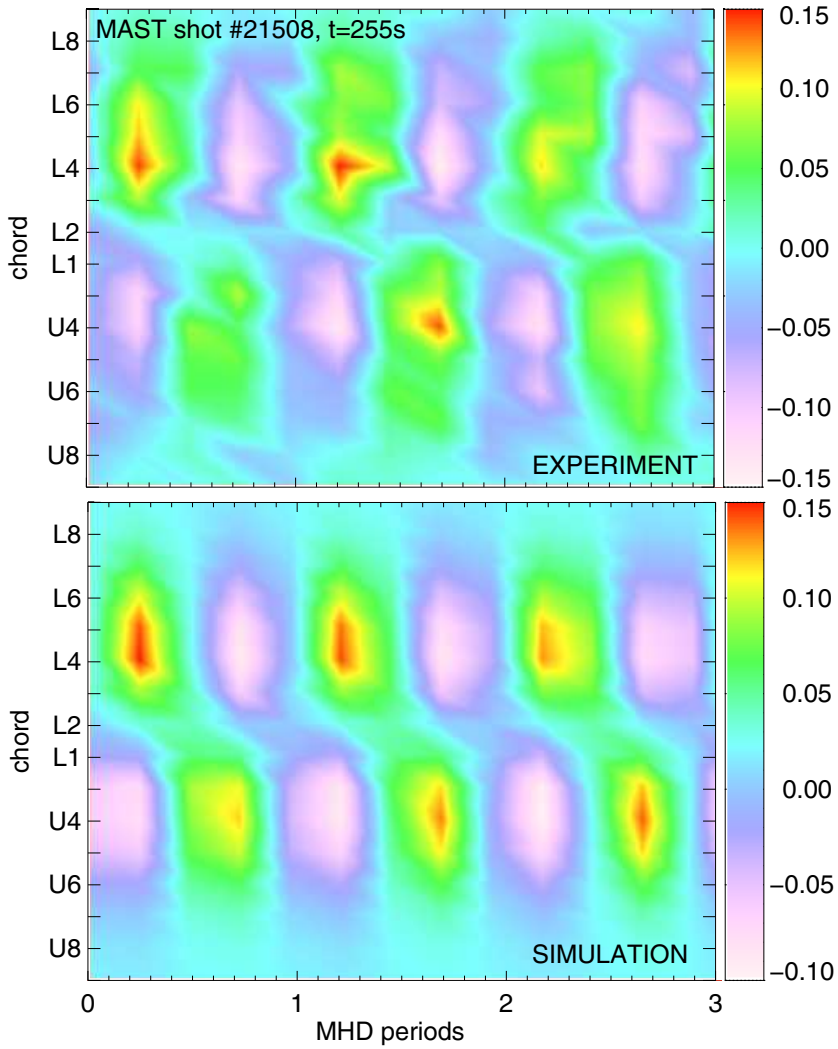

Figure 10. The experimental fluctuations caused by the MHD mode on MAST SXR horizontal array for shot 21508 at $t = 255$ms, and the simulated signal based on a radial mode amplitude of 1.2cm.

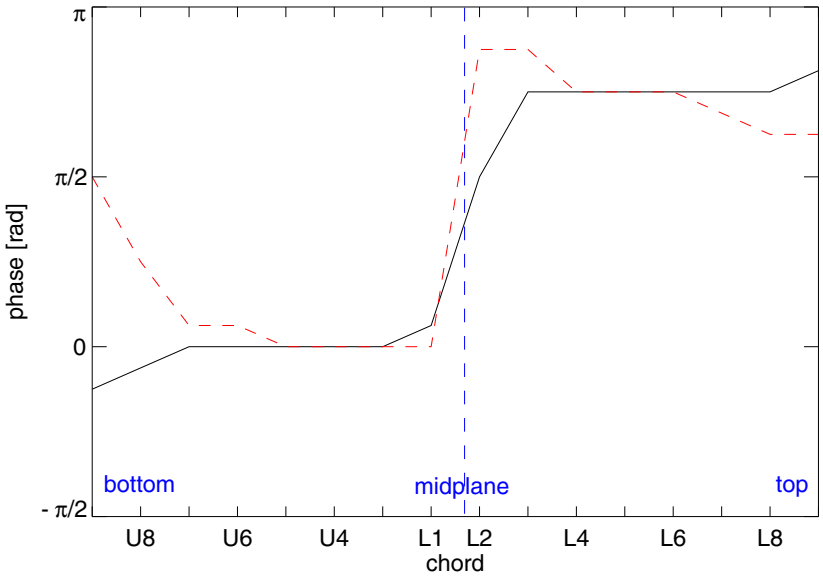

Figure 11. Relative phases of the simulated SXR chords (plain line) and the experimental ones (dashed line). Chords $U9$ to $L1$ observe from the bottom of the plasma to the mid-plane, while chords $L9$ to $L2$ observe from the top of the plasma to the mid-plane. Chord pairs $(L3, U3)$ to $(L7, U7)$ show a constant phase, which is consistent with the kink eigenstructure predicted by CASTOR.

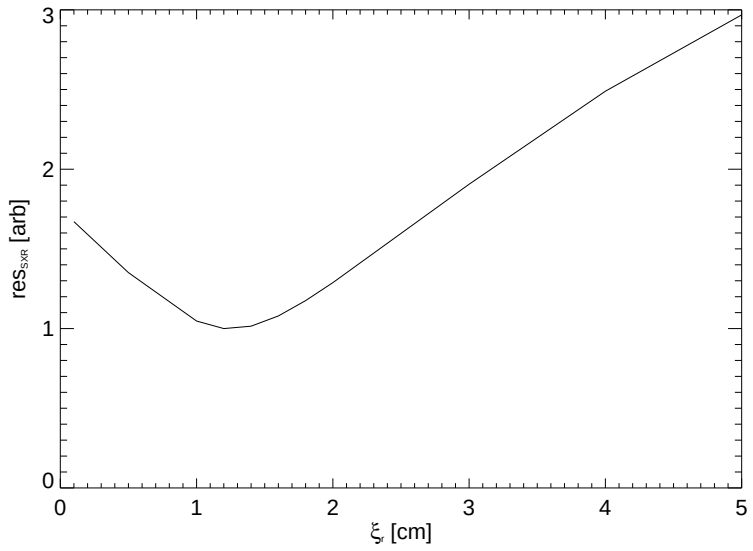

Figure 12. Residuals from the comparison between the SXR experimental measurements and the simulations for a range of perturbation amplitudes. The graph clearly shows optimal agreement for a radial amplitude of $\xi_r = 1.2$cm.

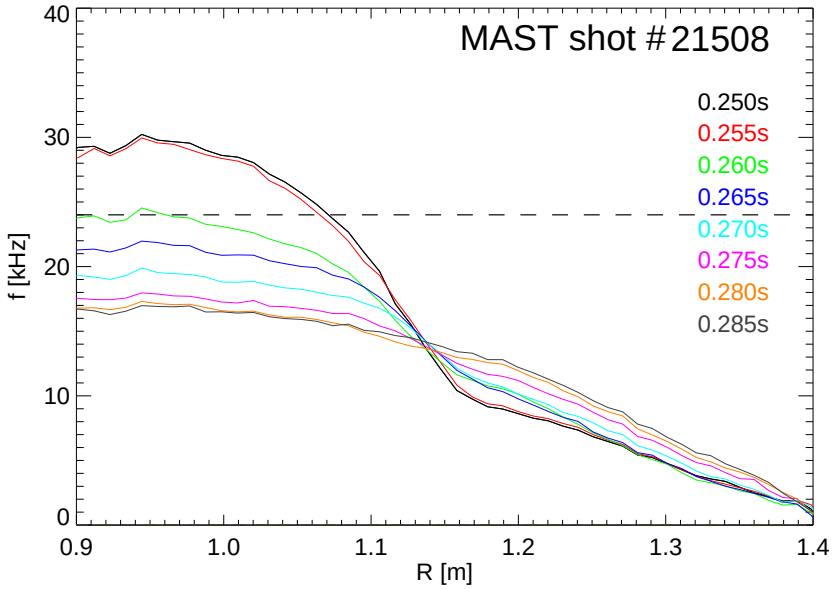

Figure 13. Profiles of plasma rotation frequency following the MHD mode onset for shot 21508. The dashed horizontal line indicates the mode frequency at $t = 255s$.

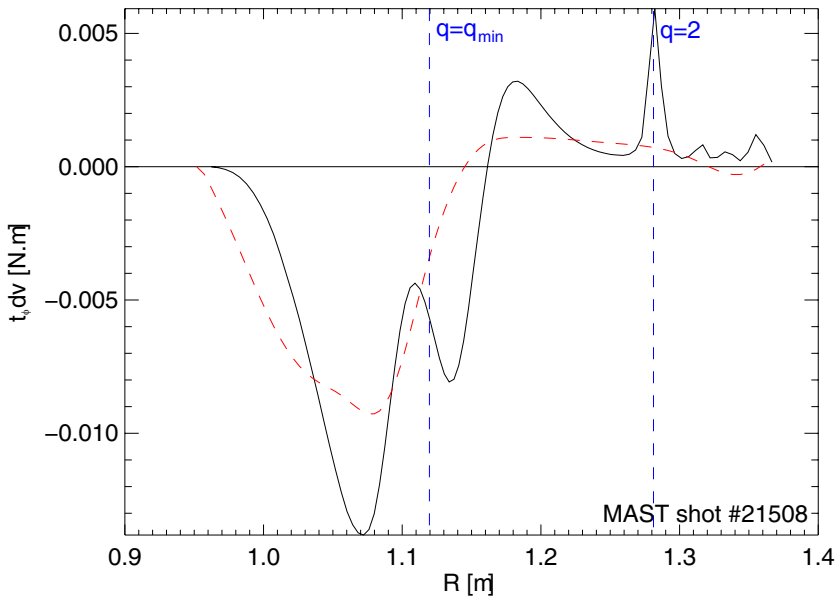

Figure 14. The torque predicted by NTV theory (plain line) and the measured rate of change of angular momentum density (dashed line) as a function of major radius for shot 21508 at $t = 255$ms.